Frontiers of Physics
https://doi.org/10.1007/s11467-020-0980-6
Front. Phys.
15(6), 63502 (2020)

RESEARCH ARTICLE

Enhancing hydrogen evolution of MoS_2 basal planes by combining single-boron catalyst and compressive strain

Zhitao Cui[1,2], Wei Du[1], Chengwei Xiao[2], Qiaohong Li[3], Rongjian Sa[4,†], Chenghua Sun[5,‡], Zuju Ma[1,#]

[1] *School of Environmental and Materials Engineering, Yantai University, Yantai 264005, China*
[2] *School of Materials Science and Engineering, Anhui University of Technology, Maanshan 243002, China*
[3] *State Key Laboratory of Structural Chemistry, Fujian Institute of Research on the Structure of Matter, Chinese Academy of Sciences, Fuzhou 350002, China*
[4] *Institute of Oceanography, Ocean College, Minjiang University, Fuzhou 350108, China*
[5] *Department of Chemistry and Biotechnology, Faculty of Science, Engineering & Technology, Swinburne University of Technology, Hawthorn, VIC 3122, Australia*
Corresponding authors. E-mail: [†] *rjsa@mju.edu.cn,* [‡] *chenghuasun@swin.edu.au,* [#] *zjma@outlook.com*
Received June 24, 2020; accepted July 12, 2020

MoS_2 is a promising candidate for hydrogen evolution reaction (HER), while its active sites are mainly distributed on the edge sites rather than the basal plane sites. Herein, a strategy to overcome the inertness of the MoS_2 basal surface and achieve high HER activity by combining single-boron catalyst and compressive strain was reported through density functional theory (DFT) computations. The *ab initio* molecular dynamics (AIMD) simulation on B@MoS_2 suggests high thermodynamic and kinetic stability. We found that the rather strong adsorption of hydrogen by B@MoS_2 can be alleviated by stress engineering. The optimal stress of −7% can achieve a nearly zero value of ΔG_H (~ −0.084 eV), which is close to that of the ideal Pt–SACs for HER. The novel HER activity is attributed to (i) the B–doping brings the active site to the basal plane of MoS_2 and reduces the band-gap, thereby increasing the conductivity; (ii) the compressive stress regulates the number of charge transfer between (H)–(B)–(MoS_2), weakening the adsorption energy of hydrogen on B@MoS_2. Moreover, we constructed a SiN/B@MoS_2 heterojunction, which introduces an 8.6% compressive stress for B@MoS_2 and yields an ideal ΔG_H. This work provides an effective means to achieve high intrinsic HER activity for MoS_2.

Keywords MoS_2, stress engineering, single-atom catalyst, HER, charge transfer, DFT, heterojunctions

1 Introduction

With the increasing depletion of fossil fuels and the deterioration of the atmospheric environment, the production of hydrogen fuel through environment-friendly electrochemical and solar-driven photoelectrochemical (PEC) water splitting has become a promising pathway to achieve sustainable energy development [1–7]. The water-splitting reaction ($H_2O \rightarrow H_2 + 1/2O_2$) is divided into two half-reactions: the oxygen evolution reaction (OER) and the hydrogen evolution reaction (HER), which occur on the anode and cathode, respectively [1, 8]. Taking HER as an example, the mechanism of reaction in an acidic environment involves three steps: (i) Generating an adsorbed hydrogen atom on the cathode (the Volmer or discharge reaction: $H^+ + e^- + * \rightarrow H^*$); (ii) the combination of two adsorbed hydrogen to produce H_2 (the Tafel reaction: $2H^* \rightarrow H_2 + 2*$); (iii) another electron reacts with the adsorbed hydrogen and another proton in the solution to form H_2 (the Heyrovsky reaction: $H^* + H^+ + e^- \rightarrow H_2 + *$) [8–11]. The high activation energies required to form the reaction intermediates on the cathode surface will inevitably create the large kinetic barriers [12]. The resulting overpotential (the potential difference between theoretical thermodynamic potential and the experimental potential) required to drive the reaction has a significant effect on HER performance and must be taken into account [13]. Therefore, how to effectively reduce the overpotential to the greatest extent has become the most critical issue for the commercialization of the HER.

Fortunately, numerous related reports have shown that the introduction of suitable catalysts can decrease the overpotential and speed HER up, maximizing the energy conversion efficiencies [14–27]. As a traditional indus-

*Special Topic: Heterojunction and Its Applications (Ed. Chenghua Sun).

trial hydrodesulfurization catalyst, MoS_2 has attracted widespread attention in recent years because of its performance tunability, low cost, and good stability [28–33]. MoS_2 has three common structures, 1T-, 3R-, and 2H-MoS_2. Among them, the semiconductor 2H–MoS_2 has the best thermodynamic stability [1, 34], which will be hereinafter referred to as MoS_2. Previous studies have shown that the basal plane of MoS_2 is usually inert for H adsorption, and only a few active sites are distributed on the edge [35, 36]. Therefore, these defects should be overcome before the large-scale application of MoS_2. So far, the initial MoS_2 optimization can be divided into two directions, one strategy to change MoS_2 monolayer nanostructures, such as vertical nanoflake [37], nanoparticles [38], nanowires [39], mesoporous films [40] or defect-rich films [41], maximum exposure edge active sites, another strategy to enhance intrinsic activity of the edge sites by atomic scale modifications, such as construction defects [36, 40] and chemical doping at edge sites [42]. Note that the basal planes constitute the vast majority of bulk materials [36]. A strategy to activate the basal plane is beneficial for maximizing the commercialization of MoS_2. Unfortunately, the relevant research is not complete.

Recently, single-atom catalysts (SACs) become a rising star in the field of catalysts, which perfectly inherit the advantages of both heterogeneous and homogeneous catalysts [43–45]. The extreme atomic utilization efficiency enables SACs to exhibit excellent catalytic performance even under low loss conditions, which is conducive to achieving the atomic economy [46]. Secondly, the active center sites of SACs are completely exposed [47]. The charge transfer effect between the active center atom and the substrate and their low coordination environment ensures the activity of SACs in various reactions [48–50]. In addition, structural simplicity facilitates precise characterization, which, in turn, helps to achieve rational SACs design at the atomic scale [44, 51]. Importantly, we noticed that MoS_2 with stable physicochemical properties is suitable as a substrate for SACs to avoid single-atom agglomeration [52]. Currently, the vast majority of SACs that have been developed are transition metal-based, such as Pt SACs [53, 54], Ru SACs [55, 56], Mo SACs [57, 58], Cu SACs [59, 60], Fe SACs [61, 62], Co SACs [63, 64] and our previous study on V SACs [52]. However, the deficiency of metal SACs including low selectivity, low faradaic efficiency, low production rate, and excessive dependence on pH must be overcome before they are widely used [65, 66]. Fortunately, Braunschweig *et al.* pioneered a new strategy for N_2 fixation based on metal-free center in 2018 [67]. However, to our knowledge, only a few metal-free SACs have been reported, such as single-boron catalyzed N_2 reduction reaction (NRR) [68–70], and single-iodine catalyzed HER [71]. Therefore, the exploitation of highly efficient metal-free SACs and their application in electrocatalytic HER will become a research hotspot in this field. Importantly, Liu *et al.* [72] emphasized that the single boron atom catalysts (B SAC) embedded in the defective MoS_2 monolayer with S vacancies may be more inclined to promote HER in their study on the SACs for NRR.

In addition, strain engineering has been proven to be a powerful strategy for regulating the electronic structure of the two-dimensional (2D) nanomaterial and optimizing the catalytic performance in recent years [73–76], which can restore the hope of many initially unpromising catalysts [77–83]. As early as 1998, Mavrikakis *et al.* [84] regulated the surface electron structure and the energy of reaction intermediates by adjusting the surface strain. Since then, many researchers have focused on adjusting surface stress to improve catalyst efficiency [82, 85–89]. Regarding a famous case of oxygen reduction reaction (ORR) on platinum, previous studies have shown that a 1% compressive strain can increase its activity by more than 300% [82, 86]. Importantly, Li *et al.* [36] pointed out in their work on activation and optimization of monolayer MoS_2 for HER by introducing S vacancies and strain that appropriate strain can significantly improve the properties of MoS_2 for HER. Similarly, Pan *et al.* [90] successfully adjusted the electronic and magnetic properties of MoS_2 nanoribbons with strain engineering, and predicted the potential applications to spintronics and photovoltaic cells.

In this work, we successfully reported for the first time a strategy to achieve high HER activity of MoS_2 basal planes by combining strain and B SAC through density functional theory (DFT) calculations. The *ab* initio molecular dynamics (AIMD) simulation on B@MoS_2 (single boron atom embedded in MoS_2 basal plane) suggests high thermodynamic stability. Through applying tunable stress, the optimal stress to obtain ideal hydrogen adsorption free energy (ΔG_H) was determined. The underlying mechanism for the novel HER performance was explored. Moreover, the IV–V/B@MoS_2heterojunction (heterojunction of the group IV–V compounds and B@MoS_2) was constructed to simulate the effect of compressive stress on the HER performance of B@MoS_2. The methodology of combining SACs and stress could be a general strategy of optimizing catalytic performance for materials beyond MoS_2.

2 Calculation methods

Our DFT calculations were performed using the generalized gradient approximation of the Perdew–Burke–Ernzerhof functional (GGA/PBE), implemented in the Vienna Ab Initio Simulation Package (VASP) [91–93]. The projector augmented wave (PAW) [91] potential was used to describe the ion-electron interactions with the valence state $2s$ and $2p$ for B, $3s$ and $3p$ for S, $4d$ and $5s$ for Mo, respectively. The thickness of the vacuum layer was fixed at 15 Å in the z-direction to prevent peri-

odic layer-to-layer interactions. A Γ-centered 3×3×1 (geometry optimization) and 5×5×1 (self-consistent energy) Monkhorst–Pack grids for the Brillouin zone sampling and cutoff energy of 500 eV for plane wave expansion were used in the calculations. In the geometry optimization, all atoms were allowed to relax in the cell until the maximal residual force and energy on each atom was less than 0.01 eV/Å and 1.0×10^{-4} eV/atom, respectively. The long-range van der Waals (vdW) interaction often has a great influence on the structure of 2D materials [94], MoS_2 being one of them [17]. In this work, Grimme's scheme (D3) [95] was used to modify the long-range dispersion interactions.

The binding energy of the B atom (E_b(B)) embedding (substitution or adsorption) on MoS_2 was calculated by the following equation:

$$E_{\mathrm{b}}(\mathrm{B}) = E_{\mathrm{B@MoS_2}} - (E_{\mathrm{MoS_2}} + E_{\mathrm{B}} - nE_{\mathrm{S}}), \quad (1)$$

where $E_{\mathrm{B@MoS_2}}$ and $E_{\mathrm{MoS_2}}$ are the total self-consistent energy of the B@MoS_2, MoS_2. E_{B} and E_{S} are the cohesive energy of the B and S atoms [96, 97]. $n = 1$ if B atom substitutes for S atom, otherwise $n = 0$. In general, the negative E_b(B) corresponds to a stable catalyst system.

Regardless of the acid solubility and alkalinity of the reaction, the overpotential of the HER is always determined by the Gibbs free energy change of the Volmer reaction ($H^+ + e^- + * \rightarrow H^*$) [8, 46]. Thus, the absolute value of ΔG_{H} is the energy barrier to be overcome for the HER [8, 98, 99]. ΔG_{H} is calculated by the following equation:

$$\Delta G_{\mathrm{H}} = \left[E_{\mathrm{H}*} + E_{\mathrm{ZPE(H}*)} - TS_{\mathrm{(H}*)}\right] - E_{(*)} - \frac{1}{2}\left[E_{(\mathrm{H_2})} + E_{\mathrm{ZPE(H_2)}} - TS_{(\mathrm{H_2})}\right], \quad (2)$$

where $E_{\mathrm{H}*}$, $E_{(*)}$ and $E_{(\mathrm{H_2})}$ are the total self-consistent energy of the H* (B@MoS_2 adsorbs one proton), * (B@MoS_2), and free H_2 molecule, respectively. E_{ZPE} and S are the zero-point energy (ZPE) and entropy, respectively. According to the method developed by Norskov and colleagues [100, 101], the free energy of ($H^+ + e^-$) has been replaced by half the chemical potential of a hydrogen molecule. For H_2, ZPE, and S can be obtained from NIST-JANAF thermochemical tables [102]. It should be noted here that the pH is assumed to be zero, which means

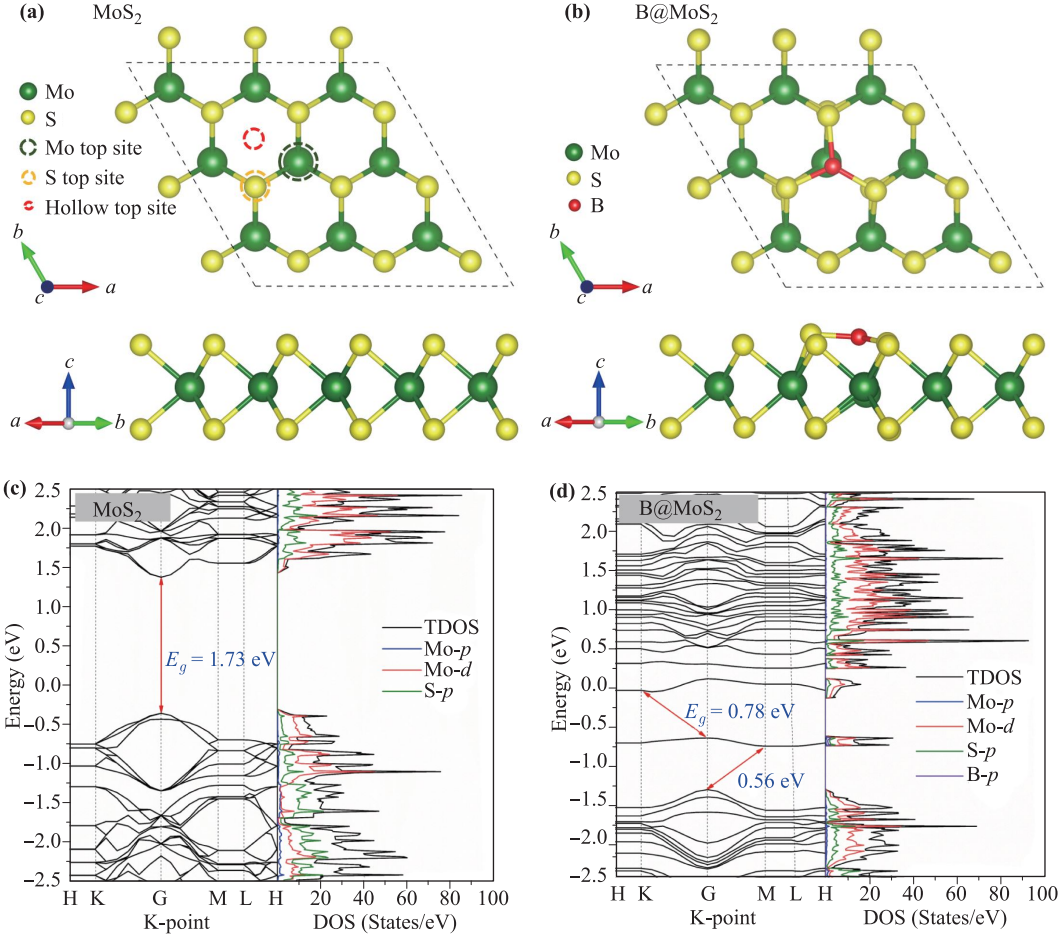

Fig. 1 The optimized structure (top and side views) and the calculated band structure and DOS of the 3 × 3 × 1 MoS_2 **(a, c)** and B@MoS_2 **(b, d)** supercell. The top view of (a) shows the sites where the B atom may be embedded (adsorbed or replaced), i.e., the Mo top site, the S top site, the hollow top site, and replacing the S atom. The Fermi level is set to zero.

the relationship between the overpotential and the pH is ignored in this work. According to the Sabatier principle, the ΔG_{H} of an ideal catalyst should be infinitely close to zero, where hydrogen is bound neither too strongly nor too weakly [103].

In addition, if the ZPE and entropy are not included in the Eq. (2), we can also obtain the adsorption energy of H^+ ($E_{ads}(H^+)$) on the surface of B@MoS_2 by the following equation:

$$E_{ads}\left(\mathrm{H}^+\right) = E_{\mathrm{H}*} - E_{(*)} - \frac{1}{2}E_{(\mathrm{H}_2)}. \tag{3}$$

3 Results and discussion

3.1 Stability and electronic structure of B@MoS_2

Based on other similar studies [104, 105], we constructed a 3 × 3 × 1 MoS_2 supercell, including 9 Mo and 18 S atoms, and optimized by GGA/PBE + D3 method which has been proved to accurately describe the geometry and electronic structure of MoS_2 [42], as shown in Fig. 1(a). Note that we also have carried out a similar study on a 4 × 4 × 1 MoS_2 supercell, and obtained consistent structural parameters and E_b(B), proving that 3 × 3 × 1 MoS_2 supercell is large enough. The lattice parameter of the primitive MoS_2 is 3.168 Å, the thickness of the monolayer is 3.2 Å, and the bond length of Mo–S bond is about 2.41 Å, which are in good agreement with the experimental report [106] and other theoretical studies [97, 107–109]. High stability is a precondition for catalysts. Strong bonding between the substrate and the supported atom is necessary to avoid the aggregation of the single atom. For the embedded B atom, we considered four typical structures, including a B atom substituting one S atom and a B atom adsorbed on top of Mo atom, S atom, and vacancy, as shown by the circle in Fig. 1(a). The most stable B@MoS_2 structure with the lowest E_b(B) of −1.607 eV is obtained, as shown in Fig. 1(b). A negative E_b(B) means that the B atom on the B@MoS_2 surface is energetically more stable than that in the bulk form [52]. The other three metastable structures and E_b(B)s are summarized in Fig. S1. Therefore, the following B@MoS_2 refers specifically to the structure of B atom adsorbing on top of Mo atom Fig. 1(b). Furthermore, the AIMD simulations on at 300 K for 10 ps with a time step of 2 fs is performed to check the thermal stability of B@MoS_2 structures [69, 96]. As shown in Fig. 2, no obvious geometry buckling of B@MoS_2 was observed during the AIMD simulations. Therefore, B@MoS_2 is thermodynamically stable.

The calculated band structure and the DOS (total density of states (TDOS) and partial density of states (PDOS)) of MoS_2 and B@MoS_2 are shown in Fig. 1(c) and Fig. 1(d), respectively. The MoS_2 behaves as a direct gap semiconductor with the band-gap energy (E_g) of 1.73 eV, which is close to the theoretical result obtained by Pan *et al.* (1.72 eV) [90]. The B-doping introduces an impurity level in the forbidden gap, which provides a new platform for electronic transitions and improves the conductivity of the catalyst. Both the conduction band minimum (CBM) and the valence band maximum (VBM) of MoS_2 and B@MoS_2 are mainly contributed by Mo-*d* and S-*p* orbitals, of which the Mo-*d* is the main component. The impurity states near the center of the forbidden band of B@MoS_2 are generated by the hybridization of B-*p* orbitals and Mo-*d* orbitals, as seen in Fig. 1(d) and Fig. 4(c).

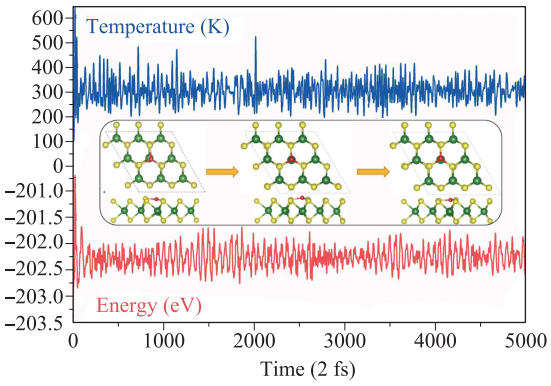

Fig. 2 The temperature and energy curve with time, in AIMD simulations for 10 ps under 300 K with a time step of 2 fs. The insert figures are the initial, intermediate, and final structure of B@MoS_2 (top and side views).

3.2 The ΔG_{H} of B@MoS_2 under stress activation and optimization

The dispersed B atoms as active sites make the inert basal plane of MoS_2 active for H^+ adsorption. According to Eq. (2), the ΔG_{H} of B@MoS_2 is calculated to be −0.451 eV, which is far from the ideal value of zero. Interestingly, previous studies showed that the process of adsorbing H^+ on the surface of MoS_2 is an endothermic reaction [36], which is converted into an exothermic spontaneous reaction after doping with B atoms (refer to Fig. S3). The loading of B SAC on MoS_2 makes it a strong absorbent for H^+, leading to the large barrier for H_2 release. We note that the electronic structure of 2D materials is sensitive to strain [13]. So, it is productive to adjust its adsorption ability towards adsorbates by strain engineering. In this work, we attempt to use this method to weaken the adsorption ability of B@MoS_2 for H^+ to activate and optimize the capacity of B@MoS_2 for HER.

The biaxially adjustable stress is simulated by changing the lattice size of the B@MoS_2, as shown in Fig. 3(a). According to the direction of stress, the strain can be divided into tensile strain and compressive strain. The stress magnitude is determined by the following equation:

$$\varepsilon = \left(\frac{L - L_0}{L_0}\right) \times 100\%, \tag{4}$$

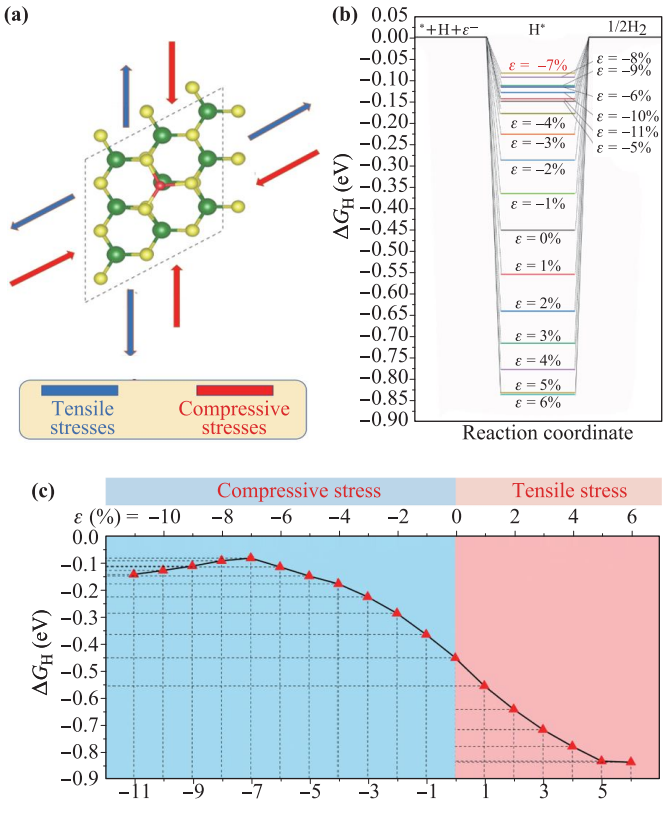

Fig. 3 **(a)** Schematic diagram of applying tunable strain to B@MoS_2. **(b)** The ΔG_H diagrams of B@MoS_2 for HER under tunable strain ($-11\% \leq \varepsilon \leq 6\%$). **(c)** The ΔG_H trend diagram with the tunable strain ($-11\% \leq \varepsilon \leq 6\%$).

where L_0 and L are the calculated supercell sizes before and after the stress application, respectively [90]. Therefore, ε is positive for tensile stress, whereas negative for compressive stress.

Since there are very stable atomic bonds in the 2D MoS_2 plane, the breaking strength is up to 18 $N{\cdot}m^{-1}$, which can sustain 11% elastic strain [110, 111]. Therefore, within the tolerable range of MoS_2, we investigated the ΔG_H under tunable strain ($-11\% \leq \varepsilon \leq 6\%$), and the result is shown in Figs. 3(b) and (c). The lattice parameter and ΔG_H data of B@MoS_2 under different stress are summarized in Tables S1 and S2. In the range of the applied strain, the adsorption of H^+ is always the spontaneous exothermic process, indicating the strong adsorption capability of B@MoS_2 for H^+. As the compressive stress increases, the adsorption capacity of B@MoS_2 for H^+ gradually decreases until $\varepsilon = -7\%$. We see that the ΔG_H corresponding to $\varepsilon = -7\%$ is closest to zero, about -0.084 eV, which is very close to that of the ideal Pt–SACs for HER (~ -0.07 eV) [53, 54]. On the contrary, as the tensile stress increases, the adsorption capacity of B@MoS_2 for H^+ continues to increase until saturation ($\varepsilon = 5\%$). Therefore, $\varepsilon = -7\%$ is the most suitable stress for B@MoS_2 to catalyze HER. In the strained B@MoS_2 with $\varepsilon = -7\%$ (-7% B@MoS_2), the Mo–S bonds are shortened under the compressive stress, but the reduction is only about 1.66%, indicating that the B@MoS_2 keeps the lattice structures [90]. In addition, the E_b(B)of -7% B@MoS_2 is determined to be -2.24 eV, which means that the -7% B@MoS_2 has certain structural stability while having the best catalytic performance.

3.3 Origins of the high HER activity on -7% B@MoS_2

We further discuss the origin of high hydrogen desorption activity of B@MoS_2 under proper compressive stress. The band structure and DOS of -7% B@MoS_2 were calculated, as shown in Fig. 4(a). The E_g of B@MoS_2 is further reduced under the action of compressive stress. The CBM and VBM are still mainly contributed by the Mo-d and S-p orbitals. Comparing Fig. 4(c) and Fig. 4(d), the contribution of B-p orbitals to the hybridization of Mo-d and B-p orbitals further increases in range of -0.75–-0.5 eV. At the same time, it is interesting that the extraneous B atom moves the Fermi energy level into the conduction band, greatly improving the conductivity of the original MoS_2, and ensuring the effective transfer of electrons in the HER process.

To associate the ΔG_H with the interaction between the substrate and adsorbed hydrogen, we illustrate the stress-dependent $E_{ads}(H^+)$ by Eq. (3) in Fig. S2. Obviously, $E_{ads}(H^+)$ and ΔG_H have the same trend with the applied stress. The $\varepsilon = -7\%$ corresponds to the weakest adsorption for H. One knows that $E_{ads}(H^+)$ is closely related to the charge transfer between the adsorbed hydrogen and the substrate. The charge density differences of B@MoS_2 and -7% B@MoS_2 before and after adsorbed hydrogen are shown in Fig. 5. Positive (electron deficit) and negative (electron excess) lobes are shown in light-blue and crimson isosurfaces, respectively. It is clear that charge redistribution occurs between the adsorbed hydrogen, fixed B atom, and MoS_2. According to the calculation results of Bader charge transfer (Table S3), we draw a schematic diagram of the charge transfer path under special stress ($\varepsilon = 0$, -7%, -11%), as shown in Fig. 6. We represent the number of transferred electrons by the red number. For all the models, B atom donates electrons to the adsorbed hydrogen and the substrate simultaneously. Compared with the stress-free B@MoS_2, the -7% compressive stress enhances the Mo-d and B-p hybridization. So, the charge transfer between B and MoS_2 rapidly increases from 0.592e to 1.01e, and the electrons obtained by adsorbed hydrogen decreases from 0.533e to 0.346e, leading to the weakened adsorption for H^+ (Fig. S2). However, as the compressive stress increases continually ($\varepsilon > -7\%$), we find that the charge transfer between B atom and MoS_2 is basically unchanged, suggesting the hybridization saturates. At the same time, the charge exchange between adsorbed hydrogen and B atom increases, and the $E_{ads}(H^+)$ is enhanced. The effect of stress on the d orbitals of the metal atom can explain this phenomenon. In general, the sp bands of

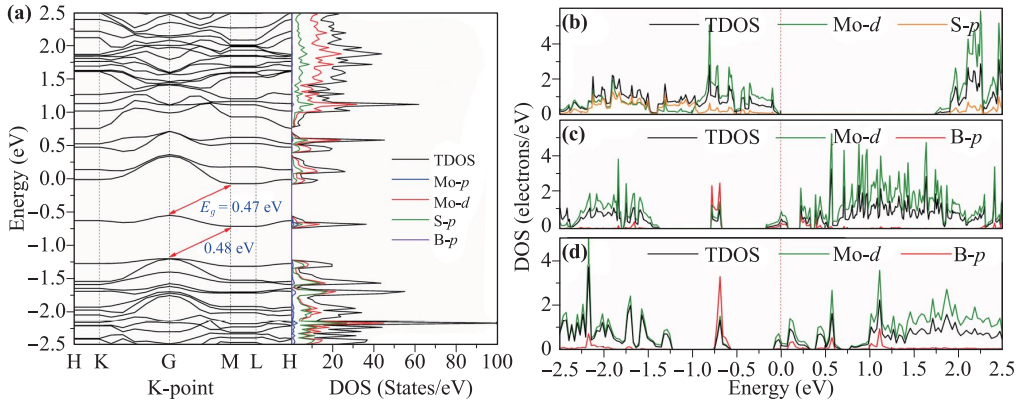

Fig. 4 **(a)** Calculated band structure and DOS of −7% B@MoS_2. The simplified DOS of MoS_2 **(b)**, B@MoS_2 **(c)**, and −7% B@MoS_2 **(d)**. Note that herein we average the DOS to each corresponding atom to get the figure. The Fermi level is set to zero.

metal are broad and structureless, while the d-band are narrow. The interaction between d states and adsorbate states can be significantly changed by even small stress changes. The compressive strain causes the Mo-d orbitals to overlap, reducing the d-band center energy [74]. Therefore, more unoccupied antibonding states are pushed below the Fermi level, allowing B to interact with them, and promoting charge transfer between B and MoS_2 [74, 112].

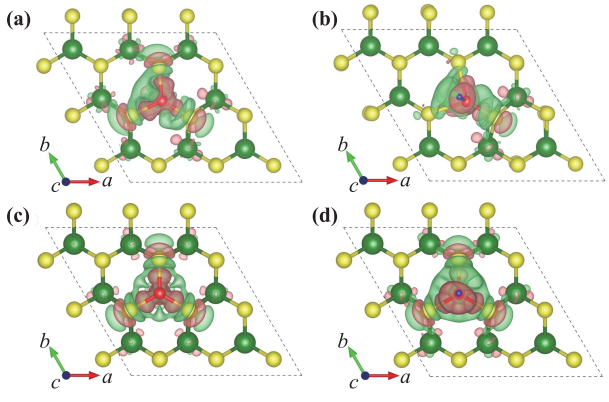

Fig. 5 The top views of the three-dimensional charge density difference plots for B@MoS_2 **(a)** and −7% B@MoS_2 **(b)**, and H^+ adsorbed B@MoS_2 **(c)** and −7% B@MoS_2 **(d)** with an isovalue of 0.004 e/Å^3. Positive (electron deficit) and negative (electron excess) lobes are shown in light-blue and crimson isosurfaces, respectively.

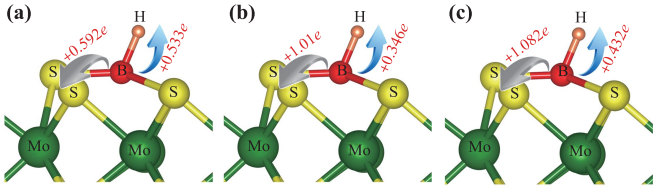

Fig. 6 Schematic diagram of the charge transfer path under ε = 0% **(a)**, ε = −7% **(b)**, and ε = −11% **(c)**. The blue and gray arrows indicate the transfer of electrons from the B atom to the adsorbed H and substrate, respectively. The "+*" denotes gaining electrons number form B atom.

When the overlap of Mo-d orbitals reaches saturation, this promotion is interrupted. Thus, the charge transfer between B atom and adsorbed hydrogen is restored.

3.4 The realization of suitable stress

The current mainstream stress realization method can be summarized as manufacturing lattice mismatch, such as generating strain through lattice mismatches of 2D material heterojunction or homojunction [13]. The idea of using the unique electronic structure of the heterojunction to reduce the overpotential of the HER has been verified by a large number of studies [113–116]. Typically, Singh *et al.* [115] carried out a study on graphene-supported TiO_2 to promote carrier photocatalytic water splitting, and the ultrathin $MoSe_2$ nanosheets coated on hollow carbon spheres synthesized by Yuan *et al.* [116] was used as high-efficiency catalysts for HER, etc. Inspired by depositing a monolayer MoS_2 grown by chemical vapor deposition (CVD) on a SiO_2 substrate with microcavities [117], we envision the growth of MoS_2 on a 2D material surface with a suitable lattice parameter. In this section, two monolayer group IV–V compounds (SiN and GeN) are examined as substrates, which have slightly smaller lattice parameters than that of B@ MoS_2 (SiN: 2.895 Å, GeN: 3.091 Å) and high theoretical stability [118]. As shown in Fig. 7, the IV–V/B@MoS_2 nano-heterojunction (GeN/B@MoS_2 and SiN/B@MoS_2) are constructed, which include 4 × 4 IV–V supercell and 4 × 4 B@MoS_2 supercell.

After full relaxation, the equilibrium distance between the IV–V layer and the B@MoS_2 layer is 3.5 Å, and the cross-sectional dimensions of two heterojunction supercells are 12.364 Å × 12.364 Å (GeN/B@MoS_2) and 11.580 Å × 11.580 Å (SiN/B@MoS_2), respectively. To evaluate the stability of the IV–V/B@MoS_2 heterojunction, the interface adhesion energy (E_{adh}) is defined according to the following equation:

$$E_{adh} = E_{\text{heter}} - E_{\text{IV-V}} - E_{\text{B@MoS}_2}, \quad (5)$$

where E_{heter}, $E_{\text{IV-V}}$, and $E_{\text{B@MoS}_2}$ are the total self-

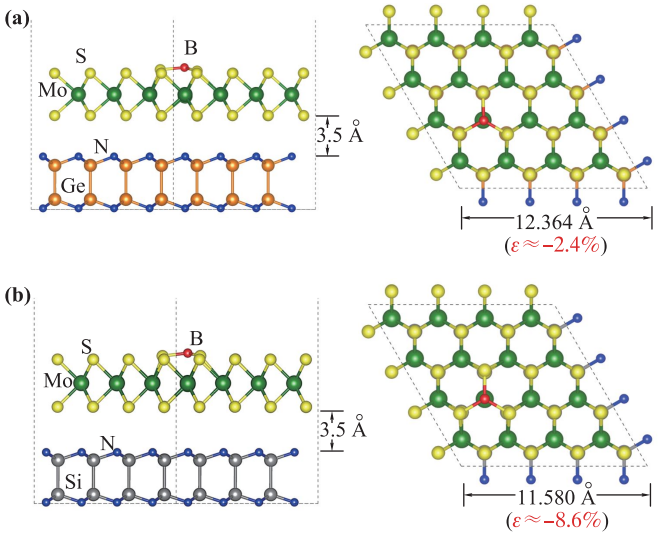

Fig. 7 Optimized GeN/B@MoS_2 **(a)** and SiN/B@MoS_2 **(b)** interface in a side view (left) and top view (right). The balls of different colors correspond to each atom type.

consistent energy of the IV–V/B@MoS_2 heterojunction, the pure IV–V, and the B@MoS_2 monolayer, respectively. The E_{adh} of IV–V/B@MoS_2 is as low as −3.376 eV (GeN/B@MoS_2) and −3.262 eV (SiN/B@MoS_2), respectively, which are stronger than the known GaS/GaSe (−1.947 eV) and graphene/MoS_2 (−0.023 eV) [119, 120]. Therefore, GeN/B@MoS_2 and SiN/B@MoS_2 are considered feasible. According to Eq. (4), the GeN/B@MoS_2 heterojunction is equivalent to applying a 2.4% compressive stress to B@MoS_2 and yields a ΔG_H of −0.281 eV, which is close to the predicted value in Fig. 3(c). Excitingly, the SiN/B@MoS_2 heterojunction is equivalent to apply an 8.6 % compressive stress to B@MoS_2 and gives a ΔG_H of −0.098 eV. It provides a theoretical basis for B@MoS_2 as an alternative to precious metal Pt–SACs for HER.

4 Conclusions

In summary, based on DFT and AIMD calculations, we designed a stable metal-free B SAC on MoS_2 (B@MoS_2) for HER. The anchored B atoms make the MoS_2 basal surface to be active for H adsorption. By optimizing stress, a compressive stress of −7% can achieve a nearly zero value of ΔG_H, about −0.084 eV, which is close to that of the ideal Pt–SACs for HER. The compressive stress regulates the number of charge transfer between (H)–(B)–(MoS_2), weakening the $E_{ads}(H^+)$ on the surface of B@MoS_2. Moreover, B doping and compressive stress reduce the bandgap and move the Fermi energy level to the conduction band, improving the conductivity of the pristine MoS_2. Finally, the SiN/B@MoS_2 heterojunction with a −8.6% compressive stress to B@MoS_2 is found to give a ΔG_H of −0.098 eV. This work not only provides an effective strategy for improving the catalytic activity of MoS_2 for HER, but also inspires more researchers to further explore and optimize the potential of metal-free SACs for HERs.

Acknowledgements This work was supported by the National Natural Science Foundation of China (Grant Nos. 21771182 and 21501177), and the Open Project Program of Structural Chemistry, Fujian Institute of Research on the Structure of Matter, Chinese Academy of Sciences. The authors also gratefully acknowledge the Supercomputing Center in Yantai university for providing the computing resources.

Supporting Information

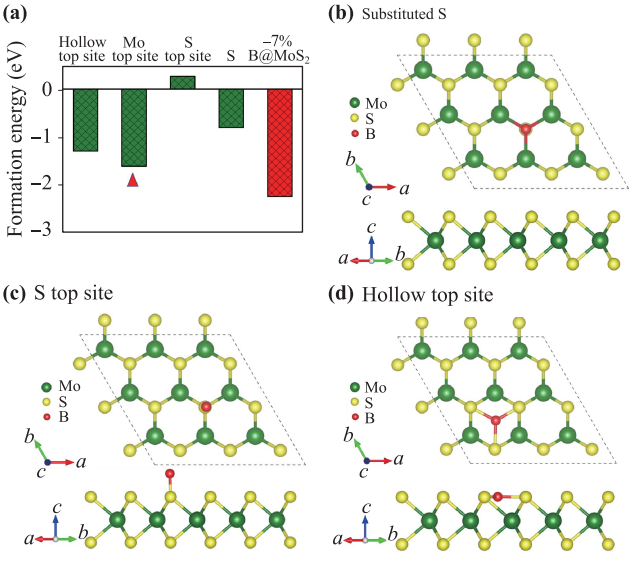

Fig. S1 **(a)** The E_b(B) of four possible structures of B@MoS_2. The top (top) and side views (bottom) of B@MoS_2 optimized structure with B atom replacing S atom **(d)** and adsorbed on the top of the vacancy **(b)**, S atoms **(c)**, respectively.

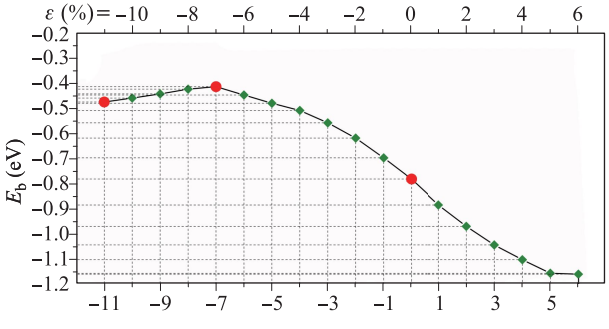

Fig. S2 The $E_{ads}(H^+)$ trend diagram with strain-tunable ($-11\% \leq \varepsilon \leq 6\%$). The red data points correspond to the three special stresses considered in Table S2.

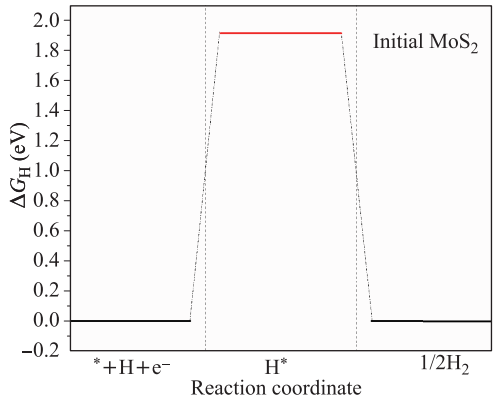

Fig. S3 Gibbs free energy diagrams of the HER on initial MoS_2 basal plane.

Table S1 The δG_H calculation data corresponding to each stress (ε), where "H" is the energy of half H_2 corrected by ZPE. Note that the H already includes the zero-point energy (ZPE) and entropy.

ε	*H	ZPE	TS	*	H	ΔG_H
−11	−195.552	0.257	0.004	−191.7	3.455	−0.144
−10	−197.801	0.256	0.005	−193.965	3.455	−0.129
−9	−199.756	0.256	0.005	−195.937	3.455	−0.113
−8	−201.432	0.256	0.005	−197.632	3.455	−0.094
−7	−202.858	0.256	0.005	−199.067	3.455	−0.084
−6	−204.084	0.256	0.004	−200.26	3.455	−0.117
−5	−205.1	0.256	0.005	−201.243	3.455	−0.15
−4	−205.913	0.256	0.005	−202.028	3.455	−0.179
−3	−206.544	0.257	0.005	−202.609	3.455	−0.227
−2	−207.009	0.257	0.005	−203.015	3.455	−0.288
−1	−207.33	0.257	0.005	−203.256	3.455	−0.366
0	−207.507	0.256	0.005	−203.35	3.455	−0.451
1	−207.547	0.256	0.005	−203.287	3.455	−0.555
2	−207.448	0.255	0.005	−203.103	3.455	−0.641
3	−207.217	0.254	0.006	−202.798	3.455	−0.716
4	−206.86	0.252	0.006	−202.382	3.455	−0.777
5	−206.381	0.251	0.006	−201.85	3.455	−0.831
6	−205.785	0.251	0.006	−201.25	3.455	−0.835

Table S2 The lattice size of the $3\times3\times1$ B@MoS_2 supercell and the corresponding δG_H under stress.

Stress (ε)	a (Å)	δG_H (eV)	Stress (ε)	a (Å)	δG_H (eV)
−11%	2.82	−0.144	−2%	3.105	−0.288
−10%	2.851	−0.129	−1%	3.137	−0.366
−9%	2.883	−0.113	0%	3.168	−0.451
−8%	2.915	−0.094	1%	3.2	−0.555
−7%	2.946	−0.084	2%	3.232	−0.641
−6%	2.978	−0.117	3%	3.263	−0.716
−5%	3.01	−0.15	4%	3.295	−0.777
−4%	3.042	−0.179	5%	3.327	−0.831
−3%	3.073	−0.227	6%	3.358	−0.835

Table S3 The δQ (in e) is the number of transferred electrons under strain-tunable via Bader charge analysis (the "+" or "−" denotes gaining or losing electrons).

ε	δQ (e)		
	MoS_2	B	Adsorbed H
0%	0.592	−1.125	0.533
−7%	1.01	−1.356	0.346
−11%	1.082	−1.514	0.432

References

1. Q. Ding, B. Song, P. Xu, and S. Jin, Efficient electrocatalytic and photoelectrochemical hydrogen generation using MoS_2 and related compounds, *Chem.* 1(5), 699 (2016)
2. J. R. McKone, N. S. Lewis, and H. B. Gray, Will solar-driven water-splitting devices see the light of day? *Chem. Mater.* 26(1), 407 (2014)
3. M. G. Walter, E. L. Warren, J. R. McKone, S. W. Boettcher, Q. Mi, E. A. Santori, and N. S. Lewis, Solar water splitting cells, *Chem. Rev.* 110(11), 6446 (2010)
4. A. J. Bard and M. A. Fox, Artificial photosynthesis: Solar splitting of water to hydrogen and oxygen, *Acc. Chem. Res.* 28(3), 141 (1995)
5. Z. Wang, J. Qin, Q. Hu, D. Wang, F. Wang, Y. Zhong, J. Zhang, H. Zhou, M. Dong, and C. Hu, Theoretical investigation of molybdenum/tungsten-vanadium solid solution alloy membranes: Thermodynamic stability and hydrogen permeation, *J. Membrane Sci.* 608, 118200 (2020)
6. Y. Zhao, F. Liu, J. Tan, P. Li, Z. Wang, K. Zhu, X. Mai, H. Liu, X. Wang, and Y. Ma, Preparation and hydrogen storage of Pd/MIL-101 nanocomposites, *J. Alloys Compounds* 772, 186 (2019)
7. Q. Chen, Q. Yin, A. Dong, Y. Gao, Y. Qian, D. Wang, M. Dong, Q. Shao, H. Liu, and B.-H. Han, Metal complex hybrid composites based on fullerene-bearing porous polycarbazole for H_2, CO_2 and CH_4 uptake and heterogeneous hydrogenation catalysis, *J. Polymer* 169, 255 (2019)
8. J. K. Nørskov, T. Bligaard, A. Logadottir, J. R. Kitchin, J. G. Chen, S. Pandelov, and U. Stimming, Trends in the exchange current for hydrogen evolution, *J. Electrochem. Soc.* 152(3), J23 (2005)
9. J. O'M. Bockris and E. C. Potter, The mechanism of the cathodic hydrogen evolution reaction, *J. Electrochem. Soc.* 99, 169 (1952)
10. B. Lin, Z. Lin, S. Chen, M. Yu, W. Li, Q. Gao, M. Dong, Q. Shao, S. Wu, T. Ding, and Z. Guo, Surface intercalated spherical $MoS_{2x}Se_{2(1-x)}$ nanocatalysts for highly efficient and durable hydrogen evolution reactions, *Dalton Trans.* 48(23), 8279 (2019)
11. Z. Lin, B. Lin, Z. Wang, S. Chen, C. Wang, M. Dong, Q. Gao, Q. Shao, T. Ding, H. Liu, S. Wu, and Z. Guo, Facile preparation of 1T/2H-Mo $(S_{1-x}Se_x)_2$ nanoparticles for boosting hydrogen evolution reaction, *ChemCatChem* 11(8), 2217 (2019)

12. T. R. Cook, D. K. Dogutan, S. Y. Reece, Y. Surendranath, T. S. Teets, and D. G. Nocera, Solar energy supply and storage for the legacy and Nonlegacy worlds, *Chem. Rev.* 110(11), 6474 (2010)
13. B. You, M. T. Tang, C. Tsai, F. Abild-Pedersen, X. Zheng, and H. Li, Enhancing electrocatalytic water splitting by strain Engineering, *Adv. Mater.* 31(17), 1807001 (2019)
14. D. Y. Chung, S. K. Park, Y. H. Chung, S. H. Yu, D. H. Lim, N. Jung, H. C. Ham, H. Y. Park, Y. Piao, S. J. Yoo, and Y. E. Sung, Edge-exposed MoS_2 nanoassembled structures as efficient electrocatalysts for hydrogen evolution reaction, *Nanoscale* 6(4), 2131 (2014)
15. H. T. Du, R. M. Kong, X. X. Guo, F. L. Qu, and J. H. Li, Recent progress in transition metal phosphides with enhanced electrocatalysis for hydrogen evolution, *Nanoscale* 10(46), 21617 (2018)
16. Y. Hong, E. L. Liu, J. Y. Shi, X. Lin, L. Z. Sheng, M. Zhang, L. Y. Wang, and J. H. Chen, A direct one-step synthesis of ultrathin g-C_3N_4 nanosheets from thiourea for boosting solar photocatalytic H_2 evolution, *Int. J. Hydrogen Energy* 44(14), 7194 (2019)
17. C. B. Ma, X. Y. Qi, B. Chen, S. Y. Bao, Z. Y. Yin, X. J. Wu, Z. M. Luo, J. Wei, H. L. Zhang, and H. Zhang, MoS_2 nanoflower-decorated reduced graphene oxide paper for high-performance hydrogen evolution reaction, *Nanoscale* 6(11), 5624 (2014)
18. Z. J. Ma, Z. T. Cui, Y. H. Lv, R. J. Sa, K. C. Wu, and Q. H. Li, Three-in-one: Opened charge-transfer channel, positively shifted oxidation potential, and enhanced visible light response of g-C_3N_4 photocatalyst through K and S Co-doping, *Int. J. Hydrogen Energy* 45(7), 4534 (2020)
19. Z. J. Ma, R. J. Sa, Q. H. Li, and K. C. Wu, Interfacial electronic structure and charge transfer of hybrid graphene quantum dot and graphitic carbon nitride nanocomposites: Insights into high efficiency for photocatalytic solar water splitting, *Phys. Chem. Chem. Phys.* 18(2), 1050 (2016)
20. Y. Pan and M. Wen, Noble metals enhanced catalytic activity of anatase TiO_2 for hydrogen evolution reaction, *Int. J. Hydrogen Energy* 43(49), 22055 (2018)
21. Z. H. Pu, I. S. Amiinu, M. Wang, Y. S. Yang, and S. C. Mu, Semimetallic MoP_2: An active and stable hydrogen evolution electrocatalyst over the whole pH range, *Nanoscale* 8(16), 8500 (2016)
22. Y. Q. Sun, L. F. Hang, Q. Shen, T. Zhang, H. L. Li, X. M. Zhang, X. J. Lyu, and Y. Li, Mo doped Ni_2P nanowire arrays: An efficient electrocatalyst for the hydrogen evolution reaction with enhanced activity at all pH values, *Nanoscale* 9(43), 16674 (2017)
23. S. Zhou, X. W. Yang, W. Pei, N. S. Liu, and J. J. Zhao, Heterostructures of MXenes and N-doped graphene as highly active bifunctional electrocatalysts, *Nanoscale* 10(23), 10876 (2018)
24. X. Li, P. Wang, Y. Q. Wu, Z. H. Liu, Q. Q. Zhang, T. T. Zhang, Z. Y. Wang, Y. Y. Liu, Z. K. Zheng, and B. B. Huang, $ZnGeP_2$: A near-infrared-activated photocatalyst for hydrogen production, *Front. Phys.* 15(2), 23604 (2020)
25. X. Zhang, X. Li, F. Jiang, W. Du, C. Hou, Z. Xu, L. Zhu, Z. Wang, H. Liu, W. Zhou, and H. Yuan, Improved electrochemical performance of 2D accordion-like MnV_2O_6 nanosheets as anode materials for Li-ion batteries, *Dalton Trans.* 49(6), 1794 (2020)
26. C. Hou, Y. Hou, Y. Fan, Y. Zhai, Y. Wang, Z. Sun, R. Fan, F. Dang, and J. Wang, Oxygen vacancy derived local build-in electric field in mesoporous hollow Co_3O_4 microspheres promotes high-performance Li-ion batteries, *J. Mater. Chem. A Mater. Energy Sustain.* 6(16), 6967 (2018)
27. C. Hou, J. Wang, W. Du, J. Wang, Y. Du, C. Liu, J. Zhang, H. Hou, F. Dang, L. Zhao, and Z. Guo, One-pot synthesized molybdenum dioxide-molybdenum carbide heterostructures coupled with 3D holey carbon nanosheets for highly efficient and ultrastable cycling lithium-ion storage, *J. Mater. Chem. A Mater. Energy Sustain.* 7(22), 13460 (2019)
28. M. Chhowalla, H. S. Shin, G. Eda, L. J. Li, K. P. Loh, and H. Zhang, The chemistry of two-dimensional layered transition metal dichalcogenide nanosheets, *Nat. Chem.* 5(4), 263 (2013)
29. M. Xu, T. Liang, M. Shi, and H. Chen, Graphene-like two-dimensional materials, *Chem. Rev.* 113(5), 3766 (2013)
30. R. R. Chianelli, M. H. Siadati, M. P. De la Rosa, G. Berhault, J. P. Wilcoxon, R. Jr Bearden, and B. L. Abrams, Catalytic properties of single layers of transition metal sulfide catalytic materials, *Catal. Rev.* 48(1), 1 (2006)
31. J. Mao, Y. Wang, Z. Zheng, and D. Deng, The rise of two-dimensional MoS_2 for catalysis, *Front. Phys.* 13(4), 138118 (2018)
32. H. M. Dong, S. D. Guo, Y. F. Duan, F. Huang, W. Xu, and J. Zhang, Electronic and optical properties of single-layer MoS_2, *Front. Phys.* 13(4), 137307 (2018)
33. J. C. Lei, X. Zhang, and Z. Zhou, Recent advances in MXene: Preparation, properties, and applications, *Front. Phys.* 10(3), 276 (2015)
34. K. F. Mak, C. Lee, J. Hone, J. Shan, and T. F. Heinz, Atomically Thin MoS_2: A new direct-gap semiconductor, *Phys. Rev. Lett.* 105(13), 136805 (2010)
35. P. Raybaud, J. Hafner, G. Kresse, S. Kasztelan, and H. Toulhoat, *Ab initio* study of the H_2+~~H_2~~ S/MoS_2 gas–solid interface: The nature of the catalytically active sites, *J. Catal.* 189(1), 129 (2000)
36. H. Li, C. Tsai, A. L. Koh, L. Cai, A. W. Contryman, A. H. Fragapane, J. Zhao, H. S. Han, H. C. Manoharan, F. Abild-Pedersen, J. K. Norskov, and X. Zheng, Activating and optimizing MoS_2 basal planes for hydrogen evolution through the formation of strained sulphur vacancies, *Nat. Mater.* 15(1), 48 (2016)
37. D. Kong, H. Wang, J. J. Cha, M. Pasta, K. J. Koski, J. Yao, and Y. Cui, Synthesis of MoS_2 and $MoSe_2$ films with vertically aligned layers, *Nano Lett.* 13(3), 1341 (2013)
38. Y. Li, H. Wang, L. Xie, Y. Liang, G. Hong, and H. Dai, MoS_2 Nanoparticles Grown on Graphene: An advanced catalyst for the hydrogen evolution reaction, *J. Am. Chem. Soc.* 133(19), 7296 (2011)

39. Z. Chen, D. Cummins, B. N. Reinecke, E. Clark, M. K. Sunkara, and T. F. Jaramillo, Core-shell MoO_3-MoS_2 nanowires for hydrogen evolution: A functional design for electrocatalytic materials, *Nano Lett.* 11(10), 4168 (2011)
40. J. Xie, H. Zhang, S. Li, R. Wang, X. Sun, M. Zhou, J. Zhou, X. W. D. Lou, and Y. Xie, Defect-rich MoS_2 ultrathin nanosheets with additional active edge sites for enhanced electrocatalytic hydrogen evolution, *Adv. Mater.* 25(40), 5807 (2013)
41. J. Kibsgaard, Z. Chen, B. N. Reinecke, and T. F. Jaramillo, Engineering the surface structure of MoS_2 to preferentially expose active edge sites for electrocatalysis, *Nat. Mater.* 11(11), 963 (2012)
42. H. Wang, C. Tsai, D. Kong, K. Chan, F. Abild-Pedersen, J. K. Nørskov, and Y. Cui, Transition-metal doped edge sites in vertically aligned MoS_2 catalysts for enhanced hydrogen evolution, *Nano Res.* 8(2), 566 (2015)
43. R. Lang, T. Li, D. Matsumura, S. Miao, Y. Ren, Y. T. Cui, Y. Tan, B. Qiao, L. Li, A. Wang, X. Wang, and T. Zhang, Hydroformylation of olefins by a rhodium single-atom catalyst with activity comparable to $RhCl(PPh_3)_3$, *Angew. Chem. Int. Ed.* 55(52), 16054 (2016)
44. P. Liu, Y. Zhao, R. Qin, S. Mo, G. Chen, L. Gu, D. M. Chevrier, P. Zhang, Q. Guo, D. Zang, B. Wu, G. Fu, and N. Zheng, Photochemical route for synthesizing atomically dispersed palladium catalysts, *Science* 352(6287), 797 (2016)
45. F. Chen, X. Jiang, L. Zhang, R. Lang, and B. Qiao, Single-atom catalysis: Bridging the homo- and heterogeneous catalysis, *Chin. J. Catal.* 39(5), 893 (2018)
46. Y. Chen, S. Ji, C. Chen, Q. Peng, D. Wang, and Y. Li, Single-atom catalysts: Synthetic strategies and electrochemical applications, *Joule* 2(7), 1242 (2018)
47. Z. W. Seh, J. Kibsgaard, C. F. Dickens, I. B. Chorkendorff, J. K. Norskov, and T. F. Jaramillo, Combining theory and experiment in electrocatalysis: Insights into materials design, *Sci* 355(6321), eaad4998 (2017)
48. L. Fan, P. F. Liu, X. Yan, L. Gu, Z. Z. Yang, H. G. Yang, S. Qiu, and X. Yao, Atomically isolated nickel species anchored on graphitized carbon for efficient hydrogen evolution electrocatalysis, *Nat. Commun.* 7(1), 10667 (2016)
49. H. T. Chung, D. A. Cullen, D. Higgins, B. T. Sneed, E. F. Holby, K. L. More, and P. Zelenay, Direct atomic-level insight into the active sites of a high-performance PGM-free ORR catalyst, *Science* 357(6350), 479 (2017)
50. Y. Chen, S. Ji, Y. Wang, J. Dong, W. Chen, Z. Li, R. Shen, L. Zheng, Z. Zhuang, D. Wang, and Y. Li, Isolated single iron atoms anchored on N-doped porous carbon as an efficient electrocatalyst for the oxygen reduction reaction, *Angew. Chem. Int. Ed.* 56(24), 6937 (2017)
51. A. Zitolo, N. Ranjbar-Sahraie, T. Mineva, J. Li, Q. Jia, S. Stamatin, G. F. Harrington, S. M. Lyth, P. Krtil, S. Mukerjee, E. Fonda, and F. Jaouen, Identification of catalytic sites in cobalt-nitrogen-carbon materials for the oxygen reduction reaction, *Nat. Mater.* 8, 957 (2017)
52. Z. Ma, Z. Cui, C. Xiao, W. Dai, Y. Lv, Q. Li, and R. Sa, Theoretical screening of efficient single-atom catalysts for nitrogen fixation based on a defective BN monolayer, *Nanoscale* 12(3), 1541 (2020)
53. J. Zhang, Y. Zhao, X. Guo, C. Chen, C. L. Dong, R. S. Liu, C. P. Han, Y. Li, Y. Gogotsi, and G. Wang, Single platinum atoms immobilized on an MXene as an efficient catalyst for the hydrogen evolution reaction, *Nat. Catal.* 1(12), 985 (2018)
54. T. He, S. M. Chen, B. Ni, Y. Gong, Z. Wu, L. Song, L. Gu, W. P. Hu, and X. Wang, Zirconium-porphyrin-based metal-organic framework hollow nanotubes for immobilization of noble-metal single atoms, *Angew. Chem. Int. Ed.* 57(13), 3493 (2018)
55. Y. Guo, S. Mei, K. Yuan, D. J. Wang, H. C. Liu, C. H. Yan, and Y. W. Zhang, Low-temperature CO_2 methanation over CeO_2-supported Ru single atoms, nanoclusters, and nanoparticles competitively tuned by strong metal-support interactions and H-spillover effect, *ACS Catal.* 8(7), 6203 (2018)
56. C. H. Zhang, J. W. Sha, H. L. Fei, M. J. Liu, S. Yazdi, J. B. Zhang, Q. F. Zhong, X. L. Zou, N. Q. Zhao, H. S. Yu, Z. Jiang, E. Ringe, B. I. Yakobson, J. C. Dong, D. L. Chen, and J. M. Tour, Single-atomic ruthenium catalytic sites on nitrogen-doped graphene for oxygen reduction reaction in acidic medium, *ACS Nano* 11(7), 6930 (2017)
57. T. Yang, T. T. Song, J. Zhou, S. J. Wang, D. Z. Chi, L. Shen, M. Yang, and Y. P. Feng, High-throughput screening of transition metal single atom catalysts anchored on molybdenum disulfide for nitrogen fixation, *Nano Energy* 68, 104304 (2020)
58. L. Han, X. Liu, J. Chen, R. Lin, H. Liu, F. Lue, S. Bak, Z. Liang, S. Zhao, E. Stavitski, J. Luo, R. R. Adzic, and H. L. Xin, Atomically dispersed molybdenum catalysts for efficient ambient nitrogen fixation, *Angew. Chem. Int. Ed.* 58(8), 2321 (2019)
59. Y. T. Qu, Z. J. Li, W. X. Chen, Y. Lin, T. W. Yuan, Z. K. Yang, C. M. Zhao, J. Wang, C. Zhao, X. Wang, F. Y. Zhou, Z. B. Zhuang, Y. Wu, and Y. D. Li, Direct transformation of bulk copper into copper single sites via emitting and trapping of atoms, *Nat. Catal.* 1(10), 781 (2018)
60. M. D. Marcinkowski, M. T. Darby, J. L. Liu, J. M. Wimble, F. R. Lucci, S. Lee, A. Michaelides, M. Flytzani-Stephanopoulos, M. Stamatakis, and E. C. H. Sykes, Pt/Cu single-atom alloys as coke-resistant catalysts for efficient C-H activation, *Nat. Chem.* 10(3), 325 (2018)
61. Y. Zhou, G. Gao, Y. Li, W. Chu, and L. W. Wang, Transition-metal single atoms in nitrogen-doped graphenes as efficient active centers for water splitting: A theoretical study, *Phys. Chem. Chem. Phys.* 21(6), 3024 (2019)
62. L. Yang, D. Cheng, X. Zeng, X. Wan, J. Shui, Z. Xiang, and D. Cao, Unveiling the high-activity origin of single-atom iron catalysts for oxygen reduction reaction, *Proc. Natl. Acad. Sci. USA* 115(26), 6626 (2018)
63. X. X. Wang, D. A. Cullen, Y. T. Pan, S. Hwang, M. Wang, Z. Feng, J. Wang, M. H. Engelhard, H. Zhang, Y. He, Y. Shao, D. Su, K. L. More, J. S. Spendelow, and G. Wu, Nitrogen-coordinated single cobalt atom catalysts for oxygen reduction in proton exchange membrane fuel cells, *Adv. Mater.* 30(11), 1706758 (2018)

64. X. J. Cui, J. P. Xiao, Y. H. Wu, P. P. Du, R. Si, H. X. Yang, H. F. Tian, J. Q. Li, W. H. Zhang, D. H. Deng, and X. H. Bao, A graphene composite material with single cobalt active sites: A highly efficient counter electrode for dye-sensitized solar cells, *Angew. Chem. Int. Ed.* 55(23), 6708 (2016)
65. Q. Tang and D. E. Jiang, Phosphorene-supported transition-metal dimer for effective N_2 electroreduction, *ChemPhysChem* 20(22), 3141 (2019)
66. Y. Cao, S. Deng, Q. Fang, X. Sun, C. Zhao, J. Zheng, Y. Gao, H. Zhuo, Y. Li, Z. Yao, Z. Wei, X. Zhong, G. Zhuang, and J. Wang, Single and double boron atoms doped nanoporous C_2N-*h*2D electrocatalysts for highly efficient N_2 reduction reaction: A density functional theory study, *Nanotechnology* 30(33), 335403 (2019)
67. M.-A. Légaré, G. Bélanger-Chabot, R. D. Dewhurst, E. Welz, I. Krummenacher, B. Engels, and H. Braunschweig, Nitrogen fixation and reduction at boron, *Science* 359(6378), 896 (2018)
68. S. Zheng, S. Li, Z. Mei, Z. Hu, M. Chu, J. Liu, X. Chen, and F. Pan, Electrochemical nitrogen reduction reaction performance of single-boron catalysts tuned by MXene substrates, *J. Phys. Chem. Lett.* 10(22), 6984 (2019)
69. C. Ling, X. Niu, Q. Li, A. Du, and J. Wang, Metal-free single atom catalyst for N_2 fixation driven by visible light, *J. Am. Chem. Soc.* 140(43), 14161 (2018)
70. K. Bhattacharyya and A. Datta, Visible light driven efficient metal free single atom catalyst supported on nanoporous carbon nitride for nitrogen fixation, *Phys. Chem. Chem. Phys.* 21(23), 12346 (2019)
71. Y. Zhao, T. Ling, S. Chen, B. Jin, A. Vasileff, Y. Jiao, L. Song, J. Luo, and S. Z. Qiao, Non-metal single-iodine-atom electrocatalysts for the hydrogen evolution reaction, *Angew. Chem. Int. Ed.* 58(35), 12252 (2019)
72. C. Liu, Q. Li, C. Wu, J. Zhang, Y. Jin, D. R. MacFarlane, and C. Sun, Single-boron catalysts for nitrogen reduction reaction, *J. Am. Chem. Soc.* 141(7), 2884 (2019)
73. B. T. Sneed, A. P. Young, and C. K. Tsung, Building up strain in colloidal metal nanoparticle catalysts, *Nanoscale* 7(29), 12248 (2015)
74. M. Luo and S. Guo, Strain-controlled electrocatalysis on multimetallic nanomaterials, *Nat. Rev. Mater.* 2(11), 17059 (2017)
75. M. Tang, L. Liu, Y. Cheng, and G. F. Ji, First-principles study of structural, elastic, and electronic properties of CeB_6 under pressure, *Front. Phys.* 10(6), 107104 (2015)
76. X. Xie, C. Ni, Z. Lin, D. Wu, X. Sun, Y. Zhang, B. Wang, and W. Du, Phase and morphology evolution of high dielectric CoO/Co_3O_4 particles with Co_3O_4 nanoneedles on surface for excellent microwave absorption application, *J. Chem. Eng.* 396, 125205 (2020)
77. E. L. Clark, C. Hahn, T. F. Jaramillo, and A. T. Bell, Electrochemical CO_2 reduction over compressively strained CuAg surface alloys with enhanced multi-carbon oxygenate selectivity, *J. Am. Chem. Soc.* 139(44), 15848 (2017)
78. Z. Lu, G. Chen, Y. Li, H. Wang, J. Xie, L. Liao, C. Liu, Y. Liu, T. Wu, Y. Li, A. C. Luntz, M. Bajdich, and Y. Cui, Identifying the active surfaces of electrochemically tuned $LiCoO_2$ for oxygen evolution reaction, *J. Am. Chem. Soc.* 139(17), 6270 (2017)
79. T. A. Maark and A. A. Peterson, Understanding strain and ligand effects in hydrogen evolution over Pd(111) surfaces, *J. Phys. Chem. C* 118(8), 4275 (2014)
80. J. R. Petrie, V. R. Cooper, J. W. Freeland, T. L. Meyer, Z. Zhang, D. A. Lutterman, and H. N. Lee, Enhanced bifunctional oxygen catalysis in strained $LaNiO_3$ perovskites, *J. Am. Chem. Soc.* 138(8), 2488 (2016)
81. B. T. Sneed, C. N. Brodsky, C. H. Kuo, L. K. Lamontagne, Y. Jiang, Y. Wang, F. Tao, W. Huang, and C. K. Tsung, Nanoscale-phase-separated Pd-Rh boxes synthesized via metal migration: An archetype for studying lattice strain and composition effects in electrocatalysis, *J. Am. Chem. Soc.* 135(39), 14691 (2013)
82. P. Strasser, S. Koh, T. Anniyev, J. Greeley, K. More, C. Yu, Z. Liu, S. Kaya, D. Nordlund, H. Ogasawara, M. F. Toney, and A. Nilsson, Lattice-strain control of the activity in dealloyed core-shell fuel cell catalysts, *Nat. Chem.* 2(6), 454 (2010)
83. H. A. Tahini, X. Tan, U. Schwingenschlogl, and S. C. Smith, Formation and migration of oxygen vacancies in $SrCoO_3$ and their effect on oxygen evolution reactions, *ACS Catal.* 6(8), 5565 (2016)
84. M. Mavrikakis, B. Hammer, and J. K. Nørskov, Effect of strain on the reactivity of metal surfaces, *Phys. Rev. Lett.* 81(13), 2819 (1998)
85. S. Alayoglu, A. U. Nilekar, M. Mavrikakis, and B. Eichhorn, Ru-Pt core-shell nanoparticles for preferential oxidation of carbon monoxide in hydrogen, *Nat. Mater.* 7(4), 333 (2008)
86. M. Du, L. Cui, Y. Cao, and A. J. Bard, Mechanoelectrochemical catalysis of the effect of elastic strain on a platinum nanofilm for the ORR exerted by a shape memory alloy substrate, *J. Am. Chem. Soc.* 137(23), 7397 (2015)
87. M. Escudero-Escribano, A. Verdaguer-Casadevall, P. Malacrida, U. Gronbjerg, B. P. Knudsen, A. K. Jepsen, J. Rossmeisl, I. E. Stephens, and I. Chorkendorff, Pt_5Gd as a highly active and stable catalyst for oxygen electroreduction, *J. Am. Chem. Soc.* 134(40), 16476 (2012)
88. H. Shi, H. Pan, Y. W. Zhang, and B. I. Yakobson, Quasiparticle band structures and optical properties of strained monolayer MoS_2 and WS_2, *Phys. Rev. B* 87(15), 155304 (2013)
89. E. Scalise, M. Houssa, G. Pourtois, V. Afanas'ev, and A. Stesmans, Strain-induced semiconductor to metal transition in the two-dimensional honeycomb structure of MoS_2, *Nano Res.* 5(1), 43 (2012)
90. H. Pan and Y. W. Zhang, Tuning the electronic and magnetic properties of MoS_2 nanoribbons by strain engineering, *J. Phys. Chem. C* 116(21), 11752 (2012)
91. P. E. Blochl, Projector augmented-wave method, *Phys. Rev. B* 50(24), 17953 (1994)
92. J. P. Perdew, K. Burke, and M. Ernzerhof, Generalized gradient approximation made simple, *Phys. Rev. Lett.* 77(18), 3865 (1996)
93. G. Kresse and D. Joubert, From ultrasoft pseudopotentials to the projector augmented-wave method, *Phys. Rev. B* 59(3), 1758 (1999)

94. A. Du, S. Sanvito, Z. Li, D. Wang, Y. Jiao, T. Liao, Q. Sun, Y. H. Ng, Z. Zhu, R. Amal, and S. C. Smith, Hybrid graphene and graphitic carbon nitride nanocomposite: Gap opening, electron-hole puddle, interfacial charge transfer, and enhanced visible light response, *J. Am. Chem. Soc.* 134(9), 4393 (2012)
95. S. Grimme, Accurate description of van der Waals complexes by density functional theory including empirical corrections, *J. Comput. Chem.* 25(12), 1463 (2004)
96. F. Li and Q. Tang, A di-boron pair doped MoS_2 (B2@MoS_2) single-layer shows superior catalytic performance for electrochemical nitrogen activation and reduction, *Nanoscale* 11(40), 18769 (2019)
97. D. Ma, W. Ju, T. Li, X. Zhang, C. He, B. Ma, Z. Lu, and Z. Yang, The adsorption of CO and NO on the MoS_2 monolayer doped with Au, Pt, Pd, or Ni: A first-principles study, *Appl. Surf. Sci.* 383, 98 (2016)
98. J. Greeley, T. F. Jaramillo, J. Bonde, I. B. Chorkendorff, and J. K. Norskov, Computational high-throughput screening of electrocatalytic materials for hydrogen evolution, *Nat. Mater.* 5(11), 909 (2006)
99. B. Hinnemann, P. G. Moses, J. Bonde, K. P. Jørgensen, J. H. Nielsen, S. Horch, I. Chorkendorff, and J. K. Nørskov, Biomimetic hydrogen evolution: MoS_2 nanoparticles as catalyst for hydrogen evolution, *J. Am. Chem. Soc.* 127(15), 5308 (2005)
100. Á. Valdés, Z.-W. Qu, G.-J. Kroes, J. Rossmeisl, and J. K. Nørskov, Oxidation and photo-oxidation of water on TiO_2 surface, *J. Phys. Chem. C* 112(26), 9872 (2008)
101. J. Rossmeisl, Z. W. Qu, H. Zhu, G. J. Kroes, and J. K. Norskov, Electrolysis of water on oxide surfaces, *J. Electroanal. Chem.* 607(1–2), 83 (2007)
102. NIST Standard Reference Database 13, https://janaf.nist.gov
103. L. Peng, X. Zheng, L. Li, L. Zhang, N. Yang, K. Xiong, H. Chen, J. Li, and Z. Wei, Chimney effect of the interface in metal oxide/metal composite catalysts on the hydrogen evolution reaction, *Appl. Catal. B* 245, 122 (2019)
104. X. Lin, W. Li, Y. Dong, C. Wang, Q. Chen, and H. Zhang, Two-dimensional metallic MoS_2: A DFT study, *Comput. Mater. Sci.* 124, 49 (2016)
105. X. Wen, S. Yu, Y. Wang, Y. Liu, H. Wang, and J. Zhao, Doping MoS_2 monolayer with nonmetal atoms to tune its electronic and magnetic properties, and chemical activity: A computational study, *New J. Chem.* 43(15), 5766 (2019)
106. D. Yang, S. J. Sandoval, W. M. Divigalpitiya, J. C. Irwin, and R. F. Frindt, Structure of single-molecular-layer MoS_2, *Phys. Rev. B* 43(14), 12053 (1991)
107. H. Cui, X. Zhang, G. Zhang, and J. Tang, Pd-doped MoS_2 monolayer: A promising candidate for DGA in transformer oil based on DFT method, *Appl. Surf. Sci.* 470, 1035 (2019)
108. D. Ma, Y. Tang, G. Yang, J. Zeng, C. He, and Z. Lu, CO catalytic oxidation on iron-embedded monolayer MoS_2, *Appl. Surf. Sci.* 328, 32871 (2015)
109. D. Ma, W. Ju, T. Li, X. Zhang, C. He, B. Ma, Y. Tang, Z. Lu, and Z. Yang, Modulating electronic, magnetic and chemical properties of MoS_2 monolayer sheets by substitutional doping with transition metals, *Appl. Surf. Sci.* 364, 181 (2016)
110. S. Bertolazzi, J. Brivio, and A. Kis, Stretching and Breaking of Ultrathin MoS_2, *ACS Nano* 5(12), 9703 (2011)
111. A. Castellanos-Gomez, M. Poot, G. A. Steele, H. S. van der Zant, N. Agrait, and G. Rubio-Bollinger, Elastic properties of freely suspended MoS_2 nanosheets, *Adv. Mater.* 24(6), 772 (2012)
112. J. K. Norskov, F. Abild-Pedersen, F. Studt, and T. Bligaard, Density functional theory in surface chemistry and catalysis, *Proc. Natl. Acad. Sci. USA* 108(3), 937 (2011)
113. B. Liu, Y. Jin, G. Xie, Z. Wang, H. Wen, N. Ren, and D. Xing, Simultaneous photo catalysis of SiC/Fe_3O_4 nanoparticles and photo-fermentation of rhodopseudomonas *sp.* nov. strain A7 for enhancing hydrogen production under visible light irradiation, *ES Energy and Environment* 1, 56 (2018)
114. P. Yang, H. Zhao, Y. Yang, P. Zhao, X. Zhao, and L. Yang, Fabrication of N, P-codoped Mo_2C/carbon nanofibers via electrospinning as electrocatalyst for hydrogen evolution reaction, *ES Materials & Manufacturing* 7, 34 (2020)
115. N. Singh, S. Jana, G. P. Singh, and R. Dey, Graphene-supported TiO_2: Study of promotion of charge carrier in photocatalytic water splitting and methylene blue dye degradation, *Adv. Compos. Hybrid Mater* 3, 127 (2020)
116. Q. Yuan, R. Wang, Q. Wang, P. Sun, R. Nie, and X. Wang, Ultrathin $MoSe_2$ nanosheets coated on hollow carbon spheres as efficient hybrid catalyst for hydrogen evolution reaction, *ES Mater. Manuf.* 2(8), 5087 (2018)
117. D. Lloyd, X. Liu, N. Boddeti, L. Cantley, R. Long, M. L. Dunn, and J. S. Bunch, Adhesion, stiffness, and instability in atomically thin MoS_2 bubbles, *Nano Lett.* 17(9), 5329 (2017)
118. J. H. Lin, H. Zhang, X. L. Cheng, and Y. Miyamoto, Single-layer group IV–V and group V–IV–III–VI semiconductors: Structural stability, electronic structures, optical properties, and photocatalysis, *Phys. Rev. B* 96(3), 035438 (2017)
119. H. R. Jappor, Electronic structure of novel GaS/GaSe heterostructures based on GaS and GaSe monolayers, *Physica B* 524, 109 (2017)
120. Y. Ma, Y. Dai, M. Guo, C. Niu, and B. Huang, Graphene adhesion on MoS_2 monolayer: An *ab initio* study, *Nanoscale* 3(9), 3883 (2011)